

Development and Optimization of A Low-Pressure Microbubble Scrubber for Air Pollutants Removal Using CFD

H. Park^{1, 2}, S. Yang¹, Y. Yoo^{1, 2}, J. Jung³, I. Moon², H. Cho^{1*}, and J. Kim^{2*}

¹ Green Materials and Processes R&D Group, Korea Institute of Industrial Technology, Ulsan 44413, Republic of Korea

² Department of Chemical and Biomolecular Engineering, Yonsei University, Seoul 03722, Republic of Korea

³ Hankook Eng Co., Ltd., Ulsan 44413, Republic of Korea

Received 24 September 2020; revised 18 April 2023; accepted 22 June 2023; published online 05 January 2024

ABSTRACT. A microbubble scrubber is a hybrid type scrubber that combines the advantages of a general scrubber with the advantages of the microbubble. Microbubble which has generally under 50 μm diameter is one of the effective ways to remove air pollutants, like PM, NO_x , and SO_x . The low-pressure microbubble (LPMB) scrubber is a low-power, high-efficiency method that uses a blower to draw flue gas into the solution and generate microbubbles in the water by using low-pressure or negative pressure. The objective of this study was to enhance the removal efficiency of air pollutants in an LPMB scrubber by determining its optimal operating conditions for generating a large number of microbubbles. To achieve this, we developed a CFD model based on a pilot-scale LPMB scrubber and conducted case studies under different operating conditions using fluid flow analysis. The case study consisted of 12 cases according to the pressure difference (1,000, 3,000, 5,000, and 7,000 Pa) between the scrubber inlet and outlet and the initial water level (-0.2, 0, and +0.2 m). The simulation results showed that the optimal operating conditions were a pressure difference of 5,000 Pa and an initial water level of -0.2 m. The removal rates of PM, NO_x , and SO_x were 99.9, 92.6, and 99.0%, respectively when operating under the optimal operating conditions of the LPMB scrubber. The results suggest that the proposed optimal operating conditions can effectively enhance the removal efficiency of the LPMB scrubber.

Keywords: microbubble, low-pressure microbubble scrubber, removing air pollutants, CFD, fluid analysis

1. Introduction

Health studies have shown a significant association between exposure to particulate matter (PM) and health risks. It has been widely reported that air pollution exposure has adverse effects on lung and cardiovascular health (Hong et al., 2007; Landreman et al., 2008; Cohen et al., 2017; Hu et al., 2020). The World Health Organization (WHO) acknowledges atmospheric pollution as a primary source of pollution exposure for humans (WHO). Further, the International Agency for Research on Cancer (IARC) classifies outdoor air pollution as carcinogenic (Group 1) (Xie et al., 2010; Parviainen et al., 2020). PM is categorized as PM_{10} and $\text{PM}_{2.5}$, according to diameter. PM_{10} is dust smaller than 10 μm , while $\text{PM}_{2.5}$ is dust smaller than 2.5 μm , including particles smaller than 1/20 ~ 1/30 the diameter of a single strand of hair (approximately 60 μm). PM is emitted as a mixture of solid and liquid particles in the air and is chemically reactive or naturally produced. It is directly released from specific emission sources, such as workplace combustion, car fuel combustion, and biocompo-

sition combustion processes. In the case of $\text{PM}_{2.5}$, secondary formation via chemical reactions of precursors, such as sulfur oxides (SO_x), nitrogen oxides (NO_x), ammonia (NH_3), and volatile organic chemicals (VOCs), in the atmosphere significantly contribute to $\text{PM}_{2.5}$ emissions (Xing et al., 2020). As SO_2 and NO_x are major precursor gases for sulfate and nitrate formation, the reduction of SO_2 and NO_x emissions is essential for secondary particle formation and $\text{PM}_{2.5}$ control (Ma et al., 2019). Many countries are tightening regulations on PM causative materials such as NO_x and SO_x to address the problem of air pollution and will continue to strengthen in the future. The European Union (EU) aims to reduce air pollutant emissions following the requirements of the amended Gothenburg Protocol and the new EU National Emission Ceilings Directive by the following amounts — SO_2 59%, NO_x 42%, NH_3 6%, NMVOCs 28%, and $\text{PM}_{2.5}$ 22% — compared with 2005 levels until 2020 (EEA, 2018). More stringent air pollutant emission standards have been implemented in the Republic of Korea since 2020 (SO_x 32%, NO_x 28%, NH_3 39%, and PM 33%).

Typical technologies used to eliminate NO_x and SO_x include selective catalytic reduction (SCR) and wet flue gas desulfurization (WFGD). SCR systems are generally found in large utility boilers, industrial boilers, and urban solid waste boilers. Recent applications include diesel engines such as those found in large ships, diesel locomotives, gas turbines, and even cars (Choi et al., 2020). The SCR of NO_x using NH_3 as a reducing agent is

* Corresponding author. Tel.: +82-52-980-6711; fax: +82-52-980-6669.
E-mail address: htcho@kitech.re.kr (H. Cho).

* Corresponding author. Tel.: +82-2-2123-2749; fax: +82-2-312-6401.
E-mail address: kjh24@yonsei.ac.kr (J. Kim).

a well-established and efficient process for the abatement of NO_x emissions (Pappas et al., 2016). SCR mainly occurs using vanadium catalysts, and is affected by SO_2 (Long et al., 2002). The presence of SO_2 inside an SCR device can lead to oxidation of SO_3 by O_2 . Further, SO_3 leads to the formation of NO_x and ammonium sulfate separated by nitrogen-based reducers injected within the engine and is attached to the device. These sulfates can deposit on the active site of the catalyst surface without decomposing in the experimental range of temperature. The occupation of the active sites by metal sulfates and ammonium sulfates will decrease the SCR activity (Park et al., 2001). SCR technology is beneficial for the removal of NO_x , but it is limited by its vulnerability to SO_x . WFGD technology is mainly used in coal-fired power plants to control SO_2 emissions. It uses natural limestone as a absorbent and interacts with SO_2 via the absorbent and flue gas, resulting in SO_2 absorption and defluorinated gypsum (Córdoba, 2015). A considerable amount of natural limestone, approximately 1.84 t is required to absorb 1 t of SO_2 in a WFGD process (Shi et al., 2017). Moreover, natural limestone is a nonrenewable resource, and its future depletion must be considered. Studies have also revealed that the operation of the WFGD system can lead to global warming due to carbon emissions induced by the decomposition of limestone (Córdoba, 2015; Rathnayake et al., 2018; Liu et al., 2020).

Both SCR and WFGD are highly effective technologies for removing NO_x and SO_x . However, several issues are associated with their use, including an inability to simultaneously remove both NO_x and SO_x compounds, a requirement of large quantities of limestone for the absorption process, and a negative environmental impact. Therefore, in this study, we focused on air pollutant removal technology using microbubbles. Bubbles are categorized as macrobubbles, microbubbles, and nanobubbles according to size. Microbubbles are tiny bubbles with a diameter of 10 ~ 50 μm and a variety of characteristic properties. These include a higher zeta potential, lower rising speed (which results in increased dispersion), smaller buoyancy, and longer retention time in liquid as compared to macrobubbles (Zhuang et al., 2016). These characteristics result in more stable microbubbles for more extended underwater periods than macrobubbles (Takahashi et al., 2007b). The pyrolytic decomposition that occurs when bubbles collapse can generate OH radicals and shock waves at the gas-liquid interface (Agarwal et al., 2011). OH radicals are more easily generated by the instantaneous excitation of ozone microbubbles during contraction and rupture occurred (Takahashi et al., 2007a). The generation of OH radicals and pressure waves increases the solubility and disinfection ability of microbubbles, allowing for the application of gas microbubbles with oxidizing power (e.g., ozone) to various water treatment processes (Sumikura et al., 2007).

Because of the advantages associated with microbubble use, it has become a popular method for pollutant removal. Lim et al. performed nitrification and denitrification experiments in single reactor using an ejector-type microbubble generator (Lim et al., 2020). Tan et al. used a combination of microbubble and deionized water to remove the oil from contaminated metallic parts (Tan et al., 2020). Nam et al. observed an improved resolution and reduced toxicity of benzo[a]pyrene resulting from microbub-

ble ozonation (Nam et al., 2019). This suggests that microbubble ozonation is a promising technique for both the chemical degradation and toxicity reduction of organic pollutants (Nam et al., 2019). In addition, microbubbles are used in the dissolved air flotation (DAF) process, which effectively clarifies wastewater by removing suspended matter such as oil or solids. Fanaie and Khiadani studied the effect of salinity on air dissolution, the size distribution of microbubbles, and the hydrodynamics of DAF systems (Fanaie and Khiadani 2020). Moreover, several studies have analyzed microbubbles using computational fluid dynamics (CFD) (Mutharasu et al., 2018; Rodrigues and Béttega, 2018; Chen et al., 2019; Rodrigues et al., 2019; Lee et al., 2020; Park et al., 2021).

Many studies have already proven that microbubbles are effective in removing contaminants. However, microbubble for applying to a commercial scale has some problems because it needs high-pressure to create microbubbles. First, the equipment and maintenance costs are expensive because it uses a compressor. Second, it is difficult to apply for large-scale processes due to capacity limits. To solve these problems, a low-pressure microbubble (LPMB) scrubber is developed for generating microbubbles using an atomizer and blower. Microbubbles play a crucial role in the LPMB scrubber in removing PM, SO_x , and NO_x , and the removal effectiveness increases with increasing microbubble generation (Yoo et al., 2021, 2023).

In this study, we derived the optimal operating conditions for an LPMB scrubber to enhance its removal efficiency of air pollutants. The removal efficiency of the LPMB scrubber is mainly dependent on the size and quantity of the microbubbles generated. To derive the optimal operating conditions for generating a large number of microbubbles, we developed a CFD model based on a pilot-scale LPMB scrubber. Using the developed CFD model, we performed fluid flow analysis inside the LPMB scrubber and conducted case studies according to different operating conditions. Finally, the derived optimal operating conditions were applied to a pilot-scale LPMB scrubber to measure PM, NO_x , and SO_x removal rates. Section 1 explains the LPMB scrubber, and Section 2 explains the geometry, mesh, and representative models used in designing CFD models. Section 3 summarizes the results of the case study based on pressure differences and initial water level. Section 4 presents the optimal operating conditions for the LPMB scrubber.

2. Low-Pressure Microbubble Scrubber

The low-pressure microbubble (LPMB) scrubber is an effective method for removing pollutants from flue gas using microbubbles in a gas-water multiphase flow. Traditional methods for generating microbubbles are typically expensive due to their reliance on high-pressure compressors, and they can be susceptible to damage and corrosion from air pollutants such as PM and NO_x . In contrast, the LPMB scrubbers use only a blower to generate microbubbles at low pressure, which requires less energy and makes it a more cost-effective method. Moreover, LPMB scrubbers have a high throughput and are therefore well-suited for commercial applications compared to other microbubble generation techniques.

The LPMB scrubber includes two venturi meters, an atomizer, and three barriers, as shown in Figure 1. The scrubber requires a certain amount of water to operate, and a blower at the outlet creates a flow inside the scrubber by drawing in air. The flow of flue gas and water relies on pressure differences induced by the blower and passed through the venturi meters and atomizer. The blower generates the water flow, causing it to change in height, and when the water reaches the atomizer and barrier, a complex bubble flow is created due to the air flow from the atomizer, the rising gas flow, and the barrier plate. Microbubbles are generated by turbulence and eddies formed as flue gas passes through the atomizer and collides with the barriers. These microbubbles effectively remove PM, SO_x and NO_x from the flue gas, leaving clean gas outside the scrubber.

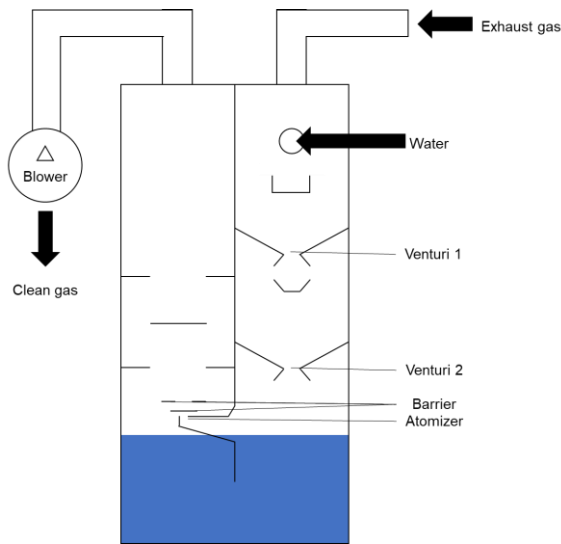


Figure 1. Schematic of a low-pressure microbubble scrubber.

3. Methods

For this study, we developed a CFD model of the LPMB scrubber. Case studies were simulated using ANSYS FLUENT and a 3.00 GHz Intel (R) Xeon(R) Gold 6136 CPU to determine the optimal operating conditions of the scrubber. In this section, we explain the geometry and mesh, and the governing equations and models used to develop the CFD model.

3.1. Geometry and Mesh

Figure 2 (a) shows the pilot-scale representation of the LPMB scrubber. The scrubber has dimensions of 1,118 × 150 × 2,100 mm (W × L × H). Figure 2 (b) shows the geometry of the LPMB scrubber for CFD modeling. The geometry was designed using ANSYS FLUENT SpaceClaim. Figure 2 (b) shows a design based on Figure 2 (a), and the same size and location were used to design the other components of the scrubber, including the venturi meters and atomizer.

Figure 3 shows the CFD model's and LPMB scrubber's mesh and includes the venturi 1, venturi 2, and the atomizer sections. These sections were selected because they experience a rapid

increase in the air velocity, and for more accurate results, a denser mesh is required. The mesh of the CFD model contains 262,192 and 1,392,227 nodes and elements, respectively. Table 1 shows the summary of the CFD model conditions. The CFD model used VOF multiphase, Realizable *k*-epsilon, and Pseudo transient. The detailed expressions for VOF multiphase, Realizable *k*-epsilon, and Pseudo transient are described in section 3.2.

Table 1. Summary of the CFD Model Conditions

Domain	Value
Model	VOF Multiphase Realizable <i>k</i> -epsilon Pseudo Transient
Gravity	-9.81 m/s ² (z-Direction)
Inlet (Gauge Pressure)	0 Pa

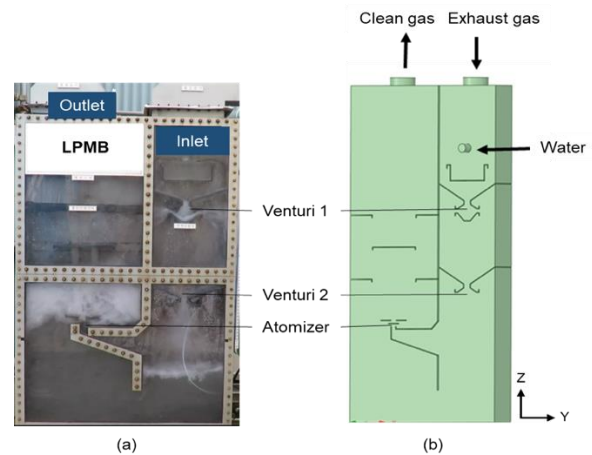


Figure 2. Low-pressure microbubble scrubber: (a) pilot-scale equipment and (b) geometry of the CFD model.

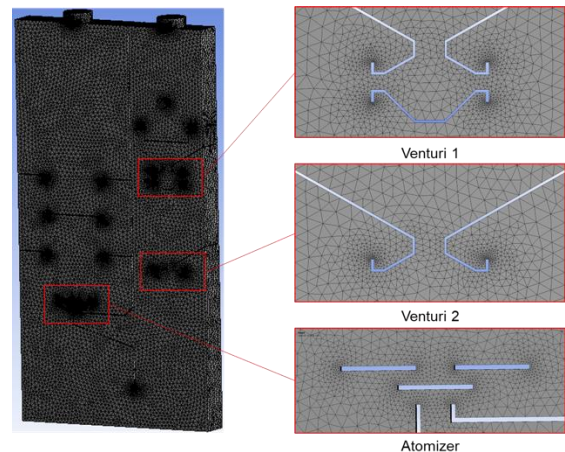


Figure 3. Mesh of the CFD model.

3.2. Governing Equations

3.2.1. Volume of the Fluid Multiphase Model

This scrubber operates in a two-phase condition: gas and liquid. Therefore, a proper multiphase model is required for flow

analysis. Currently, there are two methods for calculating multiphase flow: the Euler-Lagrange method and Euler-Euler method. The Euler-Lagrange method solves a continuum fluid phase using the Navier-Stokes equations, while the dispersed phase is traced through the calculated flow field. In the Euler-Euler method, the different phases are treated mathematically as interpenetrating continua. The conservation equations for each phase are derived to obtain a set of equations with a similar structure for all phases (ANSYS, 2013; Cho et al., 2017).

Three different Euler-Euler multiphase models are available: the volume of fluid (VOF) model, the mixture model, and the Eulerian model. The VOF model is a surface-tracking technique applied to a fixed Eulerian mesh. It is designed for two or more immiscible fluids, where the position of the interface between the fluids is of interest. In the VOF model, a single set of momentum equations is shared by the fluids, and the volume fraction of each fluid in each computational cell is tracked throughout the domain (ANSYS, 2013).

The VOF formulation relies on the fact that two or more fluids (or phases) are not interpenetrating. For each additional phase that you added to the model, a variable is introduced: the volume fraction of the phase in the computational cell. In each control volume, the volume fractions of all phases sum to unity. The fields for all variables and properties are shared by the phases and represent volume-averaged values, as long as the volume fraction of each phase is known at each location. Since the other phases cannot occupy the volume of a phase, the concept of the phasic volume fraction is introduced. These volume fractions are assumed to be continuous functions of space and time, and their sum is equal to one (ANSYS, 2013).

The tracking of the interface between the phases is accomplished by the solution of a continuity equation for the volume fraction of one of the phases. For the q^{th} phase, this equation has the following form:

$$\frac{1}{\rho_q} \left[\frac{\partial}{\partial t} (\alpha_q \rho_q) + \nabla \cdot (\alpha_q \rho_q \vec{v}_q) \right] = S_{\alpha_q} + \sum_{p=1}^n (\dot{m}_{pq} - \dot{m}_{qp}) \quad (1)$$

where \dot{m}_{qp} is the mass transfer from phase q to phase p , and \dot{m}_{qp} is the mass transfer from phase p to phase q . By default, the source term on the right-hand side of Equation (1), S_{α_q} is zero, but a constant or user-defined mass source can be specified for each phase (ANSYS, 2013).

The momentum conservation equation is as follows:

$$\frac{\partial}{\partial t} (\rho \vec{v}) + \nabla (\rho \vec{v} \vec{v}) = -\nabla p + \nabla (\bar{\tau}) + \rho \vec{g} + \vec{F} \quad (2)$$

where p is the static pressure, $\bar{\tau}$ is the stress tensor, and $\rho \vec{g}$ and \vec{F} are gravitational body force and external body force, respectively.

The stress tensor $\bar{\tau}$ is described by:

$$\bar{\tau} = \mu \left[(\nabla \vec{v} + \nabla \vec{v}^T - \frac{2}{3} \nabla \vec{v} I) \right] \quad (3)$$

where μ is the molecular viscosity, I is the unit tensor, and the second term on the right-hand side is the effect of volume dilation (ANSYS, 2013).

3.2.2. Pseudo-Transient Method

The LPMB scrubber is challenging to converge and has low stability for calculation because of its complicated structure. Therefore, we applied the pseudo-transient method to the VOF model. For steady-state VOF issues, FLUENT enables the pseudo-transient solution method and the coupled pressure-velocity scheme for improved stability and faster convergence. The pseudo transient method is a form of implicit under-relaxation. Here, the under-relaxation is controlled through the pseudo time-step size. The pseudo time-step size can be the same or different for different equations solved (ANSYS, 2013):

$$\rho_p \Delta V \frac{\phi_p - \phi_p^{old}}{\Delta t} + a_p \phi_p = \sum_{nb} a_{nb} \phi_{nb} + b \quad (4)$$

where Δt is the pseudo time step. We used the automatic time step method to estimate the pseudo time-step size for the simulation.

3.2.3. Realizable $k-\varepsilon$ Model

There are several turbulence models, including the standard $k-\varepsilon$, RNG $k-\varepsilon$, and realizable $k-\varepsilon$ models. We used a realizable $k-\varepsilon$ model to interpret the microbubbles. This model was selected based on the observations of Lee et al. (2020) that the standard model is not suitable for analyzing the microbubble volume fraction and internal flow velocity distribution (Lee et al., 2020). The realizable $k-\varepsilon$ model differs from the standard $k-\varepsilon$ model in two important ways. Firstly, the realizable $k-\varepsilon$ model contains an alternative formulation for turbulent viscosity. A modified transport equation for the dissipation rate, ε , was derived from an exact equation for the transport of the mean-square vorticity fluctuation. Secondly, the realizable $k-\varepsilon$ model satisfies certain mathematical constraints on the Reynolds stresses, consistent with the physics of turbulent flows (ANSYS, 2013; Park et al., 2022). The modeled transport equations for k and ε in the realizable $k-\varepsilon$ model are:

$$\frac{\partial}{\partial t} (\rho k) + \frac{\partial}{\partial x_j} (\rho k u_j) = \frac{\partial}{\partial x_j} \left[\left(\mu + \frac{\mu_t}{\sigma_k} \right) \frac{\partial k}{\partial x_j} \right] + G_k + G_b - \rho \varepsilon - Y_M + S_k \quad (5)$$

and

$$\frac{\partial}{\partial t} (\rho \varepsilon) + \frac{\partial}{\partial x_j} (\rho \varepsilon u_j) = \frac{\partial}{\partial x_j} \left[\left(\mu + \frac{\mu_t}{\sigma_\varepsilon} \right) \frac{\partial \varepsilon}{\partial x_j} \right] + \rho C_1 S_\varepsilon - \rho C_2 \frac{\varepsilon^2}{k + \sqrt{\nu \varepsilon}} + C_{1\varepsilon} \frac{\varepsilon}{k} C_{3\varepsilon} G_b + S_\varepsilon \quad (6)$$

where

$$C_1 = \max \left[0.43, \frac{\eta}{\eta + 5} \right], \eta = S \frac{k}{\varepsilon}, S = \sqrt{2S_{ij}S_{ij}} \quad (7)$$

In these equations, G_k represents the generation of turbulence kinetic energy due to the mean velocity gradients, calculated as described in the modeling of the turbulent production in the $k-\varepsilon$ models. G_b denotes the generation of turbulence kinetic energy due to buoyancy, calculated as described in the effects of buoyancy on turbulence in the $k-\varepsilon$ models. Y_M represents the contribution of the fluctuating dilatation in compressible turbulence to the overall dissipation rate, calculated as described in the effects of compressibility on turbulence in the $k-\varepsilon$ models. C_2 and $C_{1\varepsilon}$ are constants. σ_k and σ_ε are the turbulent Prandtl numbers for k and ε , respectively. S_k and S_ε are user-defined source terms (Lee et al., 2022; Park et al., 2022a).

4. Results and Discussion

4.1. Validation

To proceed with the case study using the developed CFD model, it was first necessary to validate that the working of the CFD model was the same as that of the actual equipment. The fluid flow of the CFD simulation and pilot-scale equipment was compared and analyzed to validate the developed CFD model.

Figure 4(a) shows the actual appearance of the operating LPMB. The scrubber operates under the pressure differences, which refers to the difference between the inlet and outlet pressures, of 5,000 Pa and a water level -0.2 m. The operation of the blower installed at the outlet lowers the pressure, creating a flow within the scrubber. The performance of the blower is implemented using the pressure differences because the scrubber operates by the blowing air at the outlet. Water level refers to the initial water height based on the atomizer before scrubber operation.

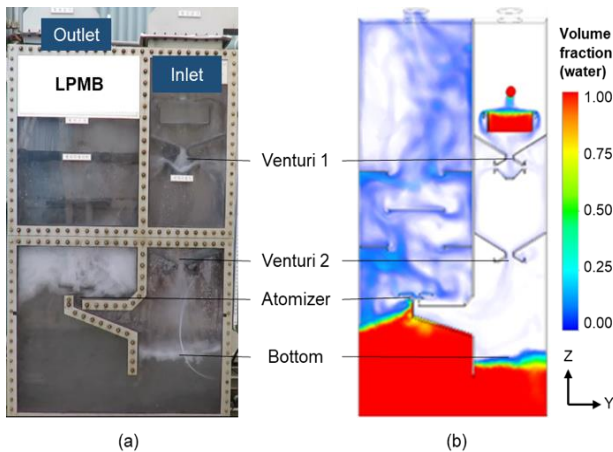


Figure 4. LPMB scrubber operating appearance: (a) pilot-scale equipment and (b) CFD model result.

Figure 4(b) shows the contour for the water volume fraction due to the simulation under actual operating conditions,

which have similar pressure differences and water level conditions to the LPMB scrubber. Red indicates water volume fraction 1, and blue indicates water volume fraction 0. The inside of the scrubber consists of two components, water and air, and the water volume fraction is 0; therefore, the air volume fraction is 1. Comparing Figure 4(a) and (b), operated under the same conditions, reveals that the same fluid flow occurs within the scrubber. When we looked at the atomizer and the bottom section, the water level changed equally after the scrubber was operated. In addition, when looking at venturi 1 and venturi 2, the shape of the water was the same. These results indicated that the CFD model was well designed, and case studies could be accurately conducted using the developed CFD model.

4.2. Case Studies

Case studies were conducted to determine the optimal operating conditions for increasing the performance of microbubble generation. Table 2 summarizes the conditions of the case studies. Case studies observed the scrubber which is changed about inlet and outlet pressure differences and the water level. Pressure differences were simulated for 1,000, 3,000, 5,000, and 7,000 Pa, and the initial water height was simulated for -0.2 , 0 , and $+0.2$ m based on the atomizer. This simulation was conducted by assuming an isothermal, and the gravity applied to the scrubber was -9.81 m/s² in the z -direction. The gauge pressure of the air entering the inlet was 0 Pa. Figure 5 shows the water volume fraction distribution of the LPMB scrubber according to the initial water level, and from the left is $+0.2$, 0 , -0.2 m respectively, based on the atomizer. The red color indicates a water volume fraction of 1 (water), and the blue indicates a fraction of 0 (air).

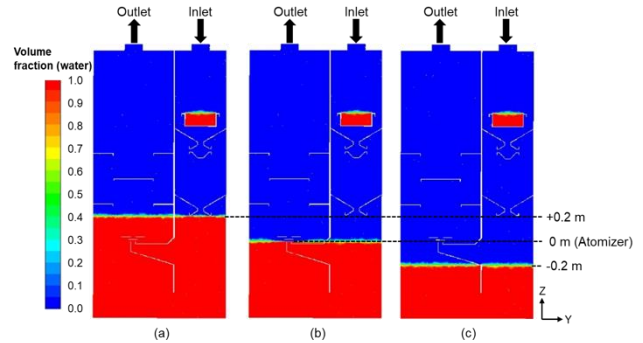


Figure 5. LPMB scrubber at an initial water level of (a) $+0.2$, (b) 0 , and (c) -0.2 m.

4.3. Simulation Results

Twelve cases were classified and simulated according to the pressure difference and initial water level. The simulation results focused on changes in the overall scrubber and key sections.

4.3.1. Results of the Overall Scrubber

In the overall scrubber, the pressure of the internal scrubber and the inlet gas flow rate changed according to the operating conditions. Figure 6 shows the pressure contours for the

12 cases divided by the pressure differences and water level. The pressure in the inlet section is was 101,325 Pa under the given conditions. Moreover, larger pressure differences yielded smaller pressures at the outlet. The pressure at the bottom of the scrubber was lowered because large pressure differences cause part of the water to rise. This also results in reduced water head pressure. Based on the water level, the bottom pressure at +0.2 m was higher than at 0 and -0.2 m in the area. This was attributed to a high water head pressure due to the significant

amount of water present inside the scrubber. The lower the initial water level, the lower the pressure in the space from the atomizer to the outlet. The LPMB scrubber produces microbubbles using negative pressure. Therefore, lower pressures inside the scrubber increase, the performance of the scrubber. In particular, the pressure in the atomizer section that produces the microbubble is essential. Figure 6 indicates that substantial pressure differences and a low water level are required to produce a significant number of microbubbles.

Table 2. Summary of Case Studies' Conditions

Case	1	2	3	4	5	6	7	8	9	10	11	12
Δ Pressure (Pa)	1,000			3,000			5,000			7,000		
Water level (m)	0.2	0.0	-0.2	0.2	0.0	-0.2	0.2	0.0	-0.2	0.2	0.0	-0.2

The gas flow rate is a crucial component of the microbubble scrubber. A high gas flow rate increases the amount of gas that can be simultaneously processed. As shown in Figure 7, changes in the water level did not influence the inlet gas flow rate but increases in pressure differences caused the rate to increase. Pressure differences are increased by improving the performance of the blower installed outside the scrubber, which activates the gas flow inside the scrubber. In addition, it was observed that the inlet gas flow rate at a water level of -0.2 m was higher than at 0 and +0.2 m, regardless of pressure differences. The only exception to this observation was case 9, which had a higher inlet gas flow rate that case 12 despite small pressure differences.

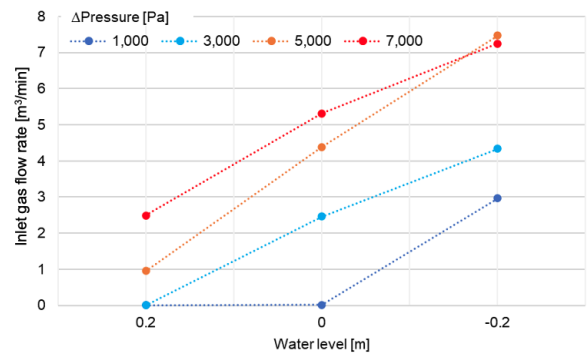


Figure 7. Inlet gas flow rates for the case studies.

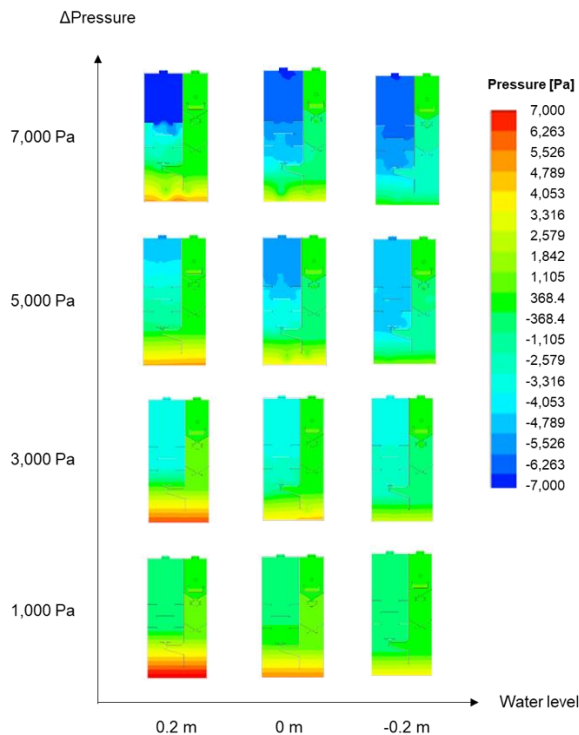


Figure 6. LPMB scrubber pressure contours according to water level and pressure differences.

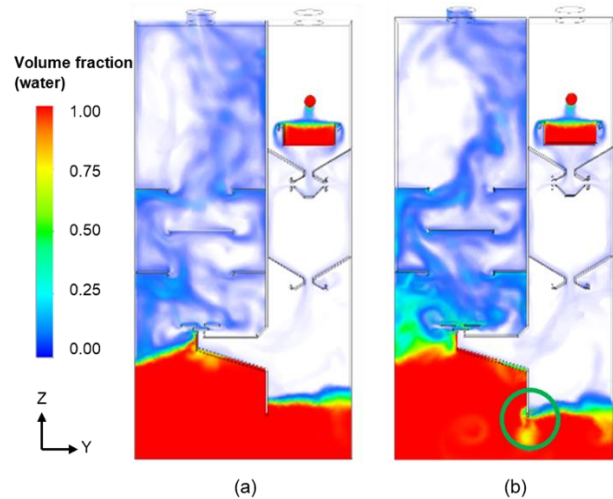


Figure 8. Contours of water volume fraction for (a) case 9 and (b) case 12. (Note: In the green circle, it can see some gas going under the wall due to the lowered water level.)

Figure 8 shows the scrubber operating in case 9 and case 12. The water level in case 12 was lower than the wall during scrubber operation. Therefore, part of the gas migrated down to the wall, and not toward the atomizer, reducing the inlet gas flow rate. These results indicate that large pressure differences or low water levels are not always beneficial to scrubber processes.

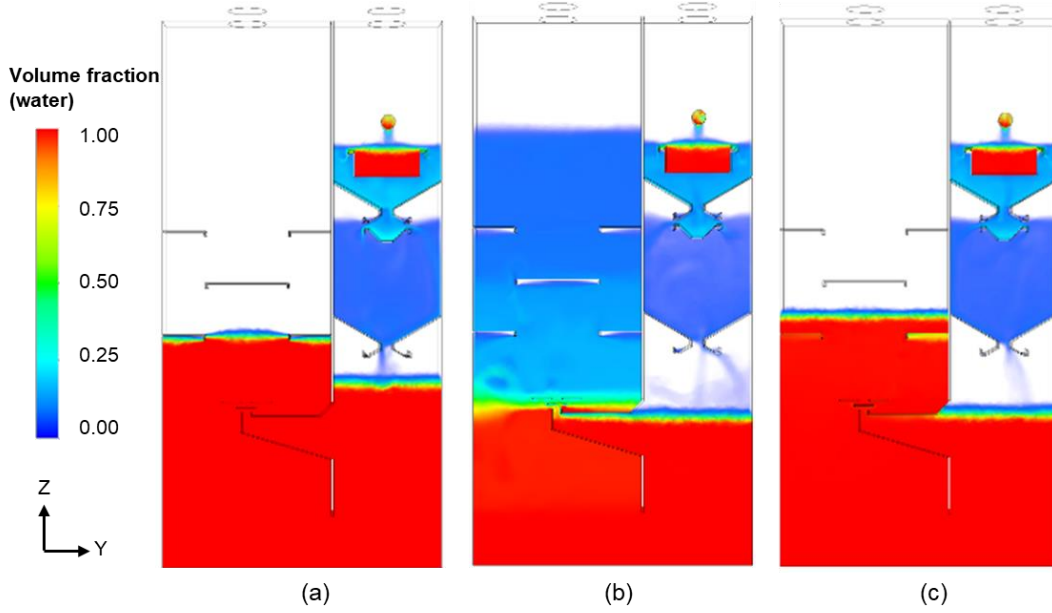


Figure 9. Contours of water volume fraction for (a) case 1, (b) case 2, and (c) case 4.

Thus, depending on the circumstances, the scrubber should be operated by selecting the appropriate operating conditions. Among the 12 cases, case 9 had the highest inlet gas flow rate of 7.4694 m³/min.

Figure 9, which displays the volume fractions for the cases, was used to determine the reason for the low (close to 0) inlet gas flow rates measured for case 1, 2, and 4. In all three cases, we observed a considerable amount of water on top of the atomizer, and the high water levels prevented water from entering the atomizer. Moreover, air could not pass through the scrubber and enter the atomizer under these conditions; therefore, microbubbles were not generated, and the measured velocity was low. Thus, it is necessary to adjust the pressure differences and water level conditions so that the water level does not rise above the atomizer during scrubber operation.

4.3.2. Results of Key Sections

There are three key sections within the LPMB scrubber: venturi 1, venturi 2, and the atomizer. Gas enters the scrubber via the inlet and moves rapidly through each of the three key sections as they contract during scrubber operation. Figures 10, 11, and 12 display the average velocities measured for the three key sections. Although the velocities showed similar trends, such as an increase with higher pressure differences and low water levels, the velocity of the gas in the atomizer moved faster than in venturi 1, venturi 2. Gas enters the inlet and passes through venturi 1, venturi 2, and atomizer before leaving the scrubber. The velocity at the venturi 1, venturi 2, and atomizer sections all have the same tendency. The higher the pressure differences and the lower the water level, the faster the average speed. But velocity at the atomizer is faster than velocity at the venturi 1 and venturi 2. A faster velocity in the atomizer is preferable as

it increases microbubbles generation. The size of the bubbles are predicted according to Equation (8) (Yin et al., 2015):

$$\frac{d}{D} = We_0(1 + c_2\alpha) \left(\frac{\sigma g_c \rho D}{\mu^2} \right)^{\frac{3}{5}} Re^{-\frac{11}{10}} \quad (8)$$

This formula indicates that the bubbles' size decreases with an increase in Re , and the velocity is closely related to Re . Thus, fast gas velocities generate microbubbles and simultaneously crush barriers effectively after passing through the atomizer. Case 9 recorded the fastest velocity in this study, which was 31.2 m/s in the atomizer.

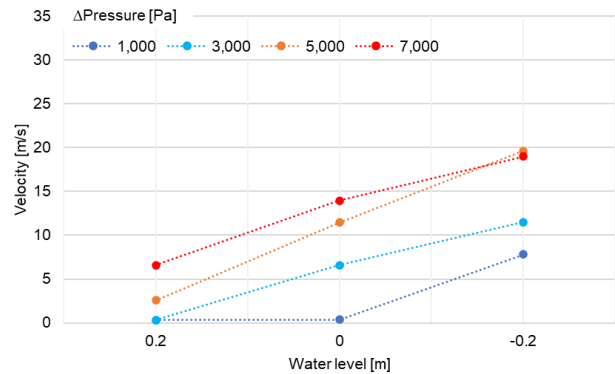


Figure 10. Velocity of the gas at the venturi 1.

Additionally, we analyzed the atomizer section, which has the most significant impact on microbubble generation. Figure 13 shows the velocity vector of the atomizer section for case 9. The flow of air to the right of the scrubber is much faster than

to the left after passing through the atomizer. Figure 14 shows the average surface velocity for case 9. From the diagram, we observed that the velocity distribution is not constant, and the red colors representing the fast velocity are distributed to the right. The difference in speed distribution is attributed to the movement of air towards the right, as it cannot exit the scrubber on the left side due to rising water levels during scrubber operation. The structure of the scrubber does not allow for the rising water levels to be controlled. The positions of the barriers were moved marginally to the right during scrubber setup to correct for air biases. This resulted in more air hitting the barriers and increased microbubbles generation.

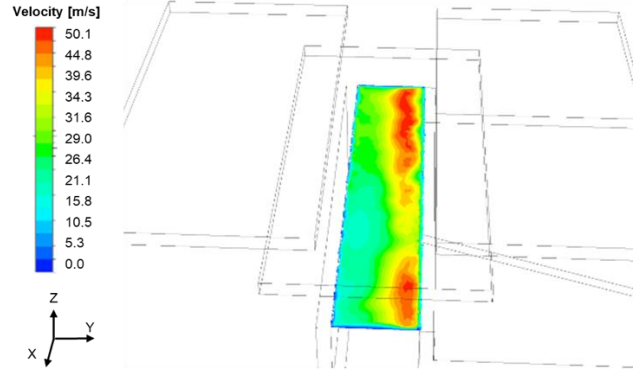


Figure 14. Velocity contour in the atomizer.

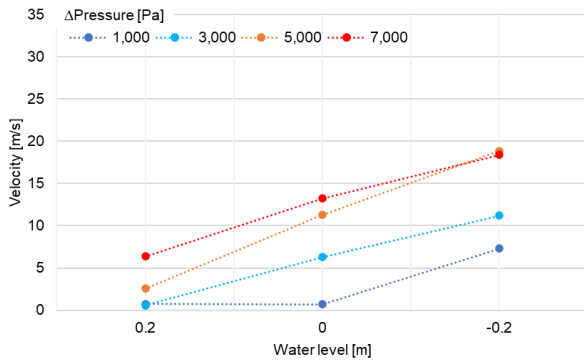


Figure 11. Velocity of the gas at the venturi 2.

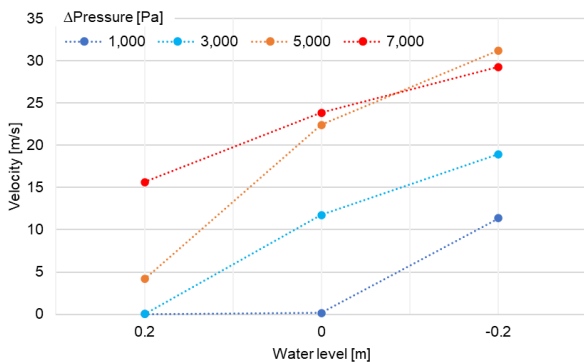


Figure 12. Velocity of gas in the atomizer.

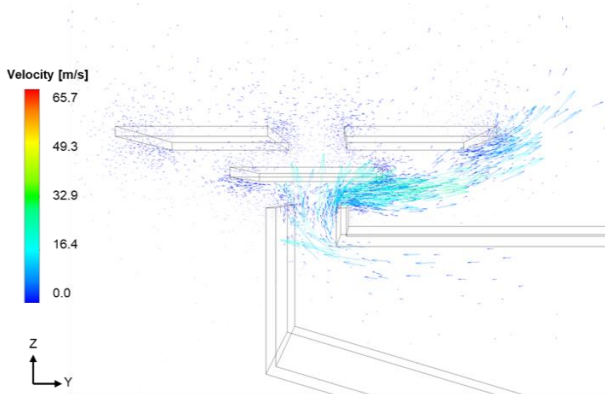


Figure 13. Velocity vector at the atomizer section.

Table 3 shows the simulation results for the inlet gas flow rate and velocity in the atomizer for the 12 cases. The results for these parameters were selected because they are considered the most important in microbubble scrubbers. The results show that larger pressure differences and lower initial water heights increase the inlet gas flow rate and velocity at the atomizer. However, when the pressure differences and the water level were beyond a certain range, the internal water level dropped to below the lower wall during scrubber operation, creating a space for air to enter and decreasing the scrubber's effectiveness. In addition, low pressure differences or very high water levels resulted in accumulation of water on the atomizer's upper section. This restricted the flow of air and reduced the inlet gas flow rate and velocity at the atomizer. High velocities of over 10 m/s were measured in the atomizer for case 3, 5, 6, and 8 ~ 12. However, case 9 recorded the highest inlet gas flow rate and velocity in the atomizer at a pressure difference of 5,000 Pa and an initial water level of -0.2 m, indicating that these are the optimal conditions for microbubble generation.

5. Conclusions

In this study, we derived the optimal operating conditions for a scrubber that utilizes low-pressure microbubble generation instead of the traditional high-pressure compressed gas method. The inlet gas flow rate and the velocity at the atomizer influence the LPMB scrubber's performance. Because they determine the flue gas treatment capacity and the microbubble size. To determine the LPMB scrubber's optimal operating conditions, we developed the CFD model based on the pilot-scale LPMB scrubber and conducted simulation case studies for 12 cases based on pressure differences (1,000, 3,000, 5,000, and 7,000 Pa) and initial water levels (-0.2, 0, and +0.2 m).

The case study showed that the larger the pressure difference, the lower the initial water level, the higher the inlet gas flow rate and velocity of the atomizer. However, pressure differences and water levels beyond a specific range cause the internal water level to drop below the lower wall during scrubber operation. This creates a space for air to enter and decreasing the scrubber's effectiveness. Therefore, proper operating conditions are required to ensure the effective operation of the scrubber. The optimal operating condition was found to be a pressure difference

Table 3. Simulation Results for the Inlet Gas Flow Rate and Velocity in the Venturi 1, Venturi 2, and Atomizer for the 12 Cases

Case	1	2	3	4	5	6	7	8	9	10	11	12
Inlet Gas Flow Rate (m ³ /min)	0.01	0.02	2.97	0.01	2.46	4.34	0.95	4.39	7.47	2.49	5.32	7.25
Velocity at Venturi 1 (m/s)	0.31	0.36	7.80	0.32	6.58	11.49	2.57	11.46	19.63	6.59	13.95	18.98
Velocity at Venturi 2 (m/s)	0.75	0.70	7.31	0.56	6.28	11.19	2.59	11.29	18.87	6.39	13.24	18.40
Velocity at Atomizer (m/s)	0.01	0.17	11.37	0.03	11.76	18.96	4.18	22.39	31.19	15.64	23.86	29.26

of 5,000 Pa and a water level of -0.2 m, which showed the highest inlet gas flow rate (7.47 m³/min) and velocity (31.19 m/s) in the atomizer. The removal rates of PM, NO_x and SO_x in the LPMB scrubber were 99.9, 92.6 and 99.0%, respectively, when the pilot-scale LPMB scrubber was operated under the optimal operating conditions derived from the CFD model, and the results were approved by the Korea Testing Laboratory (KTL) and the Korea Testing and Research Institute for Chemical Convergence (KTR).

The LPMB scrubber is an equipment that can effectively remove air pollutants at a low cost and is expected to be utilized for air pollution control in various industries. In addition, it is expected that the optimal operating conditions for each situation or scale can be derived using the method conducted in this study to effectively use LPMB scrubbers in various industries.

Acknowledgments. This work was supported by the Korea Institute of Industrial Technology within the framework of the Development of the super clean modular platform technology based on AI for eco-friendly ship to respond to IMO 2020/2050 regulations [Grant number EH-23-0016]; and Development of AI Platform for Continuous Manufacturing of Chemical Process [Grant number JH-23-0002].

References

- Agarwal, A., Ng, W.J. and Liu, Y. (2011). Principle and applications of microbubble and nanobubble technology for water treatment. *Chemosphere*, 84(9), 1175-1180. <https://doi.org/10.1016/j.chemosphere.2011.05.054>
- WHO. 9 Out of 10 People Worldwide Breathe Polluted Air, But More Countries Are Taking Action. <https://www.who.int/news/item/02-05-2018-9-out-of-10-people-worldwide-breathe-polluted-air-but-more-countries-are-taking-action>. (assessed May 2, 2018)
- ANSYS (2013). *Ansys Fluent Theory Guide, USA*. <https://kargosha.com/file/attach/201705/2812.pdf>
- Chen, A., Yang, W., Geng, S., Gao, F., He, T., Wang, Z. and Huang, Q. (2019). Modeling of microbubble flow and coalescence behavior in the contact zone of a dissolved air flotation tank using a computational fluid dynamics-population balance model. *Ind. Eng. Chem. Res.*, 58(36), 16989-17000. <https://doi.org/10.1021/acs.iecr.9b03604>
- Cho, H., Kim, J., Park, C., Lee, K., Kim, M. and Moon, I. (2017). Uneven distribution of particle flow in RFCC reactor riser. *Powder Technol.*, 312, 113-123. <https://doi.org/10.1016/j.powtec.2017.01.025>
- Choi, Y., Kim, J. and Moon, I. (2020). Simulation and economic assessment of using H₂O₂ solution in wet scrubber for large marine vessels. *Energy*, 194, 116079. <https://doi.org/10.1016/j.energy.2020.116907>
- Xie, S.H., Liu, A.L., Chen, Y.Y., Zhang, L., Zhang, H.J., Jin, B.X., Lu, W.H., Li, X.Y. and Lu, W.Q. (2010). DNA damage and oxidative stress in human liver cell L-02 caused by surface water extracts during drinking water treatment in a waterworks in China. *Environ. Mol. Mutagen.*, 51(3), 229-235. <https://doi.org/10.1002/em.20537>
- Cohen, A. J., Brauer, M., Burnett, R., Anderson, H. R., Frostad, J., Estep, K., Balakrishnan, K., Brunekreef, B., Dandona, L., Dandona, R., Feigin, V., Freedman, G., Hubbell, B., Jobling, A., Kan, H.D., Knibbs, L., Liu, Y., Martin, R., Morawska, L., Pope, C.A., Shin, H., Straif, K., Shaddick, G., Thomas, M., Van Dingenen, R., Van Donkelaar, A., Vos, T., Murray, C.J.L. and Forouzanfar, M.H. (2017). Estimates and 25-year trends of the global burden of disease attributable to ambient air pollution: An analysis of data from the global burden of diseases study 2015. *The Lancet*, 389(10082), 1907-1918. [https://doi.org/10.1016/S0140-6736\(17\)30505-6](https://doi.org/10.1016/S0140-6736(17)30505-6)
- Córdoba, P. (2015). Status of flue gas desulphurisation (FGD) systems from coal-fired power plants: Overview of the physic-chemical control processes of wet limestone FGDs. *Fuel*, 144, 274-286. <https://doi.org/10.1016/j.fuel.2014.12.065>
- Fanaie, V. R. and Khiadani, M. (2020). Effect of salinity on air dissolution, size distribution of microbubbles, and hydrodynamics of a dissolved air flotation (DAF) system. *Colloids Surf., A*, 591, 124547. <https://doi.org/10.1016/j.colsurfa.2020.124547>
- Long, R., Yang, R., and Chang R. (2002). Low temperature selective catalytic reduction (SCR) of NO with NH₃ over alternative metal oxide-based catalysts. *Chem. Comm.*, 5, 452-453, <https://doi.org/10.1039/B111382H>
- Hong, Y.C., Hwang, S.S., Kim, J.H., Lee, K.H., Lee, H.J., Lee, K.H., Lee, H.J., Lee, K.H., Yu, S.D. and Kim, D.S. (2007). Metals in particulate pollutants affect peak expiratory flow of schoolchildren. *Environ. Health Perspect.*, 115(3), 430-434. <https://doi.org/10.1289/ehp.9531>
- Hu, X.Y., He, L.C., Zhang, J.F., Qiu, X.H., Zhang, Y.P., Mo, J.H., Day, D.B., Xiang, J.B. and Gong, J.C. (2020). Inflammatory and oxidative stress responses of healthy adults to changes in personal air pollutant exposure. *Environ. Pollut.*, 263(A), 114503. <https://doi.org/10.1016/j.envpol.2020.114503>
- Landreman, A.P., Shafer, M.M., Hemming, J.C., Hannigan, M.P. and Schauer, J.J. (2008). A macrophage-based method for the assessment of the reactive oxygen species (ROS) activity of atmospheric particulate matter (PM) and application to routine (Daily-24 h) aerosol monitoring studies. *Aerosol Sci. Technol.*, 42(11), 946-957. <https://doi.org/10.1080/02786820802363819>
- Lee, J., Cho, S., Cho, H., Cho, S., Lee, I., Moon, I. and Kim, J. (2022). CFD modeling on natural and forced ventilation during hydrogen leaks in a pressure regulator process of a residential area. *Process Saf. Environ. Prot.*, 161, 436-46. <https://doi.org/10.1016/j.psep.2022.03.065>
- Lim, J. Y., Kim, H. S., Park, S. Y. and Kim, J. H. (2020). Simultaneous nitrification and denitrification by using ejector type microbubble generator in a single reactor. *Environ. Eng. Res.*, 25(2), 251-257. <https://doi.org/10.4491/eeer.2018.427>
- Liu, D., Zhu, H., Wu, K., Zhao, X., Wang, F. and Liao, Q. (2020). Assessment of waste hardened cement mortar utilization as an alternative sorbent to remove SO₂ in flue gas. *J. Hazard. Mater.*, 392, 122492. <https://doi.org/10.1016/j.jhazmat.2020.122492>
- Ma, X.Y., Jia, H.L., Sha, T., An, J.L. and Tian, R. (2019). Spatial and seasonal characteristics of particulate matter and gaseous pollution in China: implications for control policy. *Environ. Pollut.*, 248, 421-428. <https://doi.org/10.1016/j.envpol.2019.02.038>

- EEA (2018). *Environmental indicator report 2018: in support to the monitoring of the Seventh Environment Action Programme*. European Environment Agency. <https://doi.org/10.2800/180334>
- Mutharasu, L. C., Kalaga, D. V., Sathe, M., Turney, D. E., Griffin, D., Li, X.L, Kawaji, M., Nandakumar, K. and Joshi, J. B. (2018). Experimental study and CFD simulation of the multiphase flow conditions encountered in a novel down-flow bubble column. *Chem. Eng. J.*, 350, 507-522. <https://doi.org/10.1016/j.cej.2018.04.211>
- Nam, G., Mohamed, M. M. and Jung, J. (2019). Enhanced degradation of benzo[a]pyrene and toxicity reduction by microbubble ozonation. *Environ. Technol.*, 42(12), 1853-1860. <https://doi.org/10.1080/09593330.2019.1683077>
- Pappas, D. K., Boningari, T., Boolchand, P. and Smirniotis, P. G. (2016). Novel manganese oxide confined interweaved titania nano-tubes for the low-temperature selective catalytic reduction (SCR) of NO_x by NH₃. *J. Catal.*, 334, 1-13. <https://doi.org/10.1016/j.jcat.2015.11.013>
- Park, H., Lee, J., Lim, J., Cho, H. and Kim, J. (2022a). Optimal operating strategy of ash deposit removal system to maximize boiler efficiency using CFD and a thermal transfer efficiency model. *J. Ind. Eng. Chem.*, 110, 301-317. <https://doi.org/10.1016/j.jiec.2022.03.004>
- Park, H., Roh, J., Cheol Oh, K., Cho, H. and Kim, J. (2022b). Modeling and optimization of water mist system for effective air-cooled heat exchangers. *Int. J. Heat Mass Transfer*, 184, 12297. <https://doi.org/10.1016/j.ijheatmasstransfer.2021.122297>
- Park, H., Yoo, Y., Choi, Y., Roh, J., Lee, J., Kim, J. and Cho, H. (2021). Computational fluid dynamic modelling of optimal water level in low-pressure microbubbles scrubbers. *Chem. Eng. Trans.*, 86, 613-618. <https://doi.org/10.3303/CET2186103>
- Park, T. S., Jeong, S. K., Hong, S. H. and Hong, S. C. (2001). Selective catalytic reduction of nitrogen oxides with NH₃ over natural manganese ore at low temperature. *Ind. Eng. Chem. Res.*, 40(21), 4491-4495. <https://doi.org/10.1021/ie010218>
- Parviainen, A., Papanlioti, E. M., Casares-Porcel, M. and Garrido, C. J. (2020). Antimony as a tracer of non-exhaust traffic emissions in air pollution in Granada (Spain) using lichen bioindicators. *Environ. Pollut.*, 263, 114482. <https://doi.org/10.1016/j.envpol.2020.114482>
- Rathnayake, M., Julnipitawong, P., Tangtermsirikul, S. and Toochinda, P. 2018. Utilization of coal fly ash and bottom ash as solid sorbents for sulfur dioxide reduction from coal fired power plant: life cycle assessment and applications. *J. Cleaner Prod.*, 202, 934-945. <https://doi.org/10.1016/j.jclepro.2018.08.204>
- Rodrigues, J. P., Batista, J. N. M. and Béttega, R. (2019). Application of population balance equations and interaction models in CFD simulation of the bubble distribution in dissolved air flotation. *Colloids Surf., A*, 577, 723-732. <https://doi.org/10.1016/j.colsurfa.2019.06.032>
- Rodrigues, J. P. and Béttega, R. (2018). Evaluation of multiphase CFD models for dissolved air flotation (DAF) process. *Colloids Surf., A*, 539, 116-123. <https://doi.org/10.1016/j.colsurfa.2017.12.015>
- Shi, W.X., Lin, C., Chen, W., Hong, J.L., Chang, J.C., Dong, Y. and Zhang, Y.L. (2017). Environmental effect of current desulfurization technology on fly dust emission in China. *Renewable Sustainable Energy Rev.* 72, 1-9. <https://doi.org/10.1016/j.rser.2017.01.033>
- Sumikura, M., Hidaka, M., Murakami, H., Nobutomo, Y. and Murakami, T. (2007). Ozone micro-bubble disinfection method for wastewater reuse system. *Water Sci. Technol.*, 56(5), 53-61. <https://doi.org/10.2166/wst.2007.556>
- Takahashi, M., Chiba, K. and Li, P. (2007a). Formation of hydroxyl radicals by collapsing ozone microbubbles under strongly acidic conditions. *J. Phys. Chem. B*, 111(39), 11443-11446. <https://doi.org/10.1021/jp074727m>
- Takahashi, M., Chiba, K. and Li, P. (2007b). Free-Radical generation from collapsing microbubbles in the absence of a dynamic stimulus. *J. Phys. Chem. B*, 111(6), 1343-1347. <https://doi.org/10.1021/jp0669254>
- Tan, K. A., Mohan, Y., Liew, K. J., Chong, S. H. and Poh, P. E. (2020). "Development of an effective cleaning method for metallic parts using microbubbles." *J. Cleaner Prod.*, 261, 121076. <https://doi.org/10.1016/j.jclepro.2020.121076>
- Xing, J., Zheng, S.X., Ding, D., Kelly, J. T., Wang, S.X., Li, S.W., Qin, T., Ma, M.Y., Dong, Z.X., Jang, C., Zhu, Y., Zheng, H.T., Ren, L., Liu, T.Y. and Hao, J.M. (2020). Deep learning for prediction of the air quality response to emission changes. *Environ. Sci. Technol.*, 54(14), 8589-8600. <https://doi.org/10.1021/acs.est.0c02923>
- Yin, J., Li, J., Li, H., Liu, W. and Wang, D. (2015). Experimental study on the bubble generation characteristics for an venturi type bubble generator. *Int. J. Heat Mass Transfer*, 91, 218-224. <https://doi.org/10.1016/j.ijheatmasstransfer.2015.05.076>
- Yoo, Y., Park, H., Choi, Y., Jung, J., Song, H., Kim, J. and Cho, H. (2021). Method for determining optimum operational conditions of microbubble scrubber using image processing. *J. Environ. Inf.*, 38(2), 83-92. <https://doi.org/10.3808/jei.202100457>
- Yoo, Y., Ga, S., Kim, J. and Cho, H. (2023). Method for measuring bubble size under low-light conditions for mass transfer enhancement in industrial-scale systems *Int. Commun. Heat Mass Transfer*, 140, 106525. <https://doi.org/10.1016/j.icheatmasstransfer.2022.106525>
- Zhuang, H., Hong, X., Han, H. and Shan, S. (2016). Effect of pure oxygen fine bubbles on the organic matter removal and bacterial community evolution treating coal gasification wastewater by membrane bioreactor. *Bioresour. Technol.*, 221, 262-269. <https://doi.org/10.1016/j.biortech.2016.09.029>